Single-Crystalline Aluminum Nanostructures on a Semiconducting GaAs Substrate for Ultraviolet to Near-Infrared Plasmonics

Hsuan-Wei Liu,[†] Fan-Cheng Lin,[‡] Shi-Wei Lin,[†] Jau-Yang Wu,[†] Bo-Tsun Chou,[†] Kuang-Jen Lai,[†] Sheng-Di Lin,[†] and Jer-Shing Huang*[,‡,§]

[†]Department of Electronics Engineering, National Chiao Tung University, Hsinchu 30010, Taiwan and [‡]Department of Chemistry, and [§]Frontier Research Center on Fundamental and Applied Sciences of Matters, National Tsing Hua University, Hsinchu 30010, Taiwan

ABSTRACT Aluminum, as a metallic material for plasmonics, is of great interest because it extends the applications of surface plasmon resonance into the ultraviolet (UV) region and is superior to noble metals in natural abundance, cost, and compatibility with modern semiconductor fabrication processes. Ultrasmooth single-crystalline metallic films are beneficial for the fabrication of high-definition plasmonic nanostructures, especially complex integrated nanocircuits. The absence of surface corrugation and crystal boundaries also guarantees superior optical properties and applications in nanolasers. Here, we present UV to near-infrared plasmonic resonance of single-crystalline aluminum nanoslits and nanoholes. The high-definition nanostructures are fabricated with focused ion-beam milling into an ultrasmooth single-crystalline aluminum film grown on a semiconducting GaAs substrate with a molecular beam epitaxy method. The single-crystalline aluminum film shows improved reflectivity and reduced two-photon photoluminescence (TPPL) due to the ultrasmooth surface. Both linear scattering and nonlinear TPPL are studied in detail. The nanoslit arrays show clear Fano-like resonance, and the nanoholes are found to support both photonic modes and localized surface plasmon resonance. We also found that TPPL generation is more efficient when the excitation polarization is parallel rather than perpendicular to the edge of the aluminum film. Such a counterintuitive phenomenon is attributed to the high refractive index of the GaAs substrate. We show that the polarization of TPPL from aluminum preserves the excitation polarization and is independent of the crystal orientation of the film or substrate. Our study gains insight into the optical property of aluminum nanostructures on a high-index semiconducting GaAs substrate and illustrates a practical route to implement plasmonic devices onto semiconductors for future hybrid nanodevices.

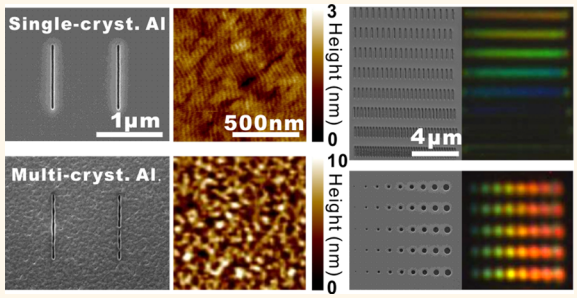

KEYWORDS: surface plasmon resonance · ultraviolet plasmonics · molecular beam epitaxy · single-crystalline aluminum · semiconducting substrate · photoluminescence · nanoholes · nanoslits

Resonant plasmonic nanostructures can concentrate light and enhance subwavelength light–matter interactions.[1,2] In recent years, surface plasmon resonance in nanostructures has been proposed and applied to achieve optical frequency integrated nanocircuits,[3−5] high-performance photovoltaic devices,[6] ultrasensitive biochemical sensors,[7,8] enhanced circular dichroism,[9] optical trapping,[10,11] efficient steam generation,[12] hot electron generation,[13] and ultrasmall color filters.[14] Silver and gold are typical plasmonic materials for the visible (vis) to infrared spectral regime, and the methods for their chemical synthesis are well-studied.[15,16] Silver has relatively low loss in the visible range but suffers from rapid degradation. Gold has good chemical stability but is more lossy than silver. In particular, the interband transition of gold around 2.3 eV limits its applications in the blue to violet spectral window. In general, the application of silver and gold in the ultraviolet (UV) spectral regime is restricted by the loss due to strong absorption of interband transition.[1] Recently, there have been considerable efforts in nonmetal plasmonics using materials such as graphene,[17,18] doped semiconductors,[19] or nitride materials.[20,21] However, none of these materials can

* Address correspondence to jshuang@mx.nthu.edu.tw.

Received for review December 12, 2014 and accepted March 24, 2015.

Published online April 07, 2015
10.1021/nn5070887

practically support surface plasmon resonance in the UV regimes. To extend the frequency window of plasmonics into the UV regime, materials like Ga, Sn, and Pb have been proposed.[22] However, aluminum is still considered to be a better material for the middle-UV range and has been used experimentally.[23−27] From the perspective of light−matter interactions, aluminum plasmonics is useful because it offers nanoscale confinement and enhancement of electromagnetic energy in the UV regime, where electronic transition with energy difference larger than 3.0 eV occurs. In addition, the nonlinear optical response of aluminum is also much larger compared to that of gold and silver, making aluminum a suitable material for higher harmonic generation. From a point of view of industrial production, aluminum is advantageous because it has relatively high natural abundance, is low-cost, and is compatible with the well-developed CMOS[28] and semiconductor manufacturing processes. These advantages make aluminum a promising material for future integration and mass production of plasmonic−semiconducting hybrid nanodevices with ultrahigh operational frequency in the UV regime and subwavelength footprints at the nanoscale.

Aluminum plasmonic nanostructures are mainly prepared by electron-beam lithography or focused-ion-beam (FIB) milling into thermally evaporated multicrystalline aluminum films. The random crystal grains and surface roughness of the multicrystalline aluminum film can directly lead to structural defects and increase the scattering loss of surface plasmons.[29,30] Compared to gold and silver films, evaporated aluminum films usually show poorer quality even at the optimal evaporation condition. The low film quality makes it very difficult to fabricate complex nanocircuits containing multiple circuit elements and greatly limits the application of aluminum, for example, in plasmonic nanolasers, which requires an ultrasmooth surface of metallic film.[31] To improve the film quality, efforts have been made by optimizing the thermal evaporation conditions.[32,33] However, the random orientation and boundaries of crystal grains in the multicrystalline aluminum film still hamper the fabrication precision and product yield. This is because, in multicrystalline metallic films, randomly oriented crystal grains lead to variation in the resistance to the ion-beam milling process. The resulting structural defects are unpredictable and are particularly fatal to large-area plasmonic nanocircuits containing multiple elements or critical fine features. This difficulty is common for all multicrystalline films, including smooth metal films prepared by a template stripping method.[34] The only way to resolve this problem is to use uniform single-crystalline films, which are naturally atomically flat. In fact, the crystal boundaries and voids inside the metal can also lead to variation of the optical properties,[35] which limits the realization of optimally designed plasmonic nanostructures. The benefits of using single-crystalline aluminum/metallic films with well-defined and well-known crystalline structure are more than just providing an ultrasmooth surface. The well-defined lattice orientation is crucial for the study and applications that concern the band structure or facet-dependent properties, such as chemical bonding and surface catalytic ability. For these reasons, using atomically flat single-crystalline aluminum film to fabricate high-definition plasmonic nanostructures is of fundamental benefit and practical importance.

Although single-crystalline gold and silver microplates from chemical synthesis have been used to fabricate high-definition plasmonic nanodevices,[30,36,37] the chemical method for the synthesis of microscale single-crystalline aluminum plates is still missing. In this work, we employ a molecular beam epitaxy (MBE) method to grow a high-quality single-crystalline aluminum film on top of the GaAs substrate and apply FIB milling to define plasmonic nanostructures, including periodic nanoslit arrays and nanoholes. Periodic nanoslit arrays and nanoholes are used because they are well-studied systems for characterizing surface plasmon polaritons (SPPs) and localized surface plasmon resonance (LSPR). Both linear scattering spectrum and nonlinear two-photon photoluminescence (TPPL) of the nanostructures are systematically studied. The effect of high-index GaAs substrate on the plasmonic resonance of aluminum nanostructures is also studied. Our work gains insight into the optical property of single-crystalline aluminum nanostructures on high-index semiconducting GaAs substrates and demonstrates the potential of single-crystalline aluminum in UV to near-infrared (NIR) plasmonics.

RESULTS AND DISCUSSION

Structural and Optical Property of Single-Crystalline Aluminum Film. Our single-crystalline aluminum film is prepared following our previously reported procedure.[38] Briefly, a GaAs buffer layer (thickness = 200 nm) is first grown on an undoped GaAs substrate in an ultrahigh vacuum chamber (3×10^{-10} Torr) to ensure a perfectly smooth (100) crystalline surface of GaAs. An aluminum film with the crystalline surface of (110) (Figure S1, Supporting Information) is then grown *in situ* on the (100) surface of the GaAs buffer layer using a solid-source MBE system (Gen II, Varian). The growing process is controlled at a constant temperature of 0 °C, and the growth rate is kept at 0.05 nm/s until the thickness of the aluminum film reaches 40 nm. For comparison, multicrystalline aluminum film is prepared by an electron-gun evaporator with a growth rate of 0.05 nm/s. Figure 1a shows the representative scanning electron microscope (SEM) images of slits and holes created by FIB milling into the single- and multicrystalline aluminum films. The multicrystalline film has been carefully and optimally prepared using an electron-gun evaporator. With the

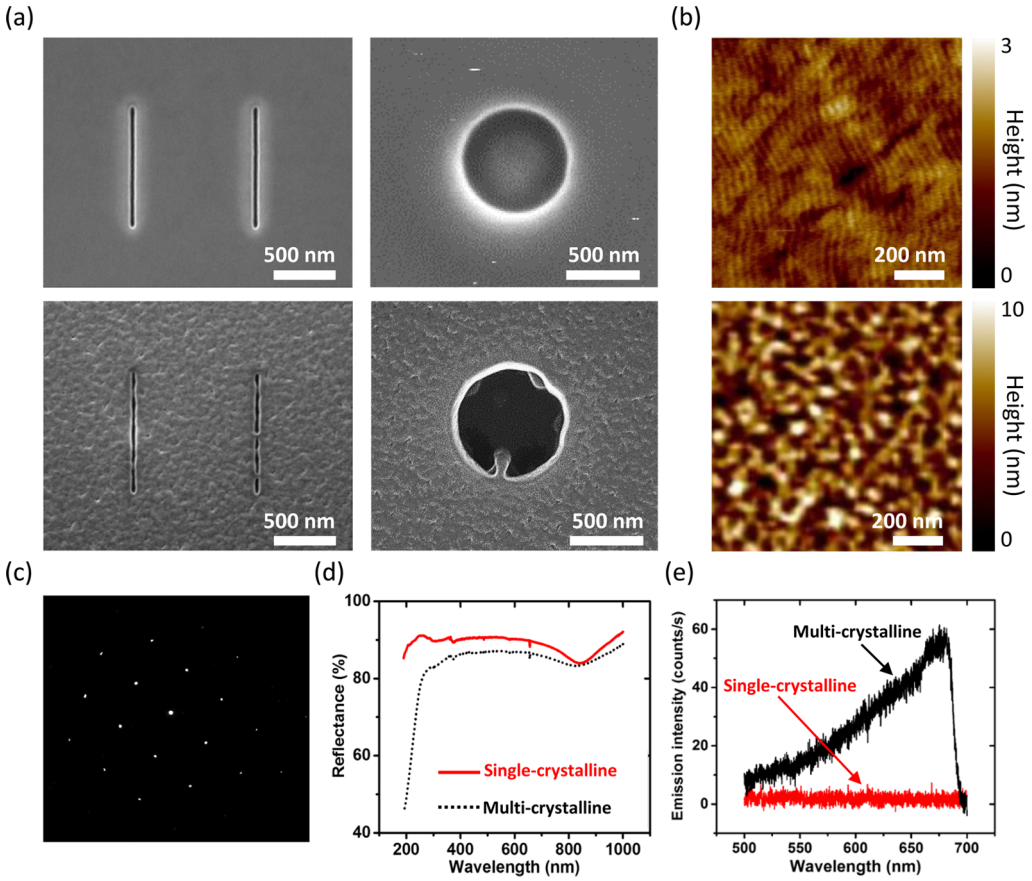

Figure 1. (a) Representative SEM images of nanoslits and holes created by FIB milling into the single- (top) and multicrystalline (bottom) aluminum film on a GaAs substrate. The ion-beam condition has been optimized for both cases in order to achieve a gap size of 30 nm. The random grains and voids of rough multicrystalline film lead to structural imperfections. Scale bar: 500 nm. (b) Representative AFM images of an area of 1 × 1 μm^2 on the single- (top) and multicrystalline (bottom) aluminum film. The root-mean-square roughness of the surface of single- and multicrystalline film is 0.3 and 2.5 nm, respectively. Scale bar: 200 nm. (c) SAED pattern of the single-crystalline aluminum film. The pattern is taken from the cross section of the aluminum film on the GaAs substrate. (d) Reflectance of the single-crystalline (red solid line) and multicrystalline (black dotted line) aluminum film. (e) TPPL spectra of single-crystalline (red) and multicrystalline (black) aluminum film under the same excitation laser power (4.5 mW on sample).

same best optimized FIB conditions at 30 kV and 80 pA, we are able to reproducibly create nanoslits with a gap width of about 30 nm on both films. However, the slits created on the multicrystalline film apparently have irregular edges and parts not clearly cut through. These defects are due to the inevitable rough surface and random crystal grains of the evaporated multicrystalline film. To better compare the surface roughness, atomic force microscopy (AFM) has been used to map an area of 1 × 1 μm^2 on the surface of both films, as shown in Figure 1b. It is clear that the MBE-grown single-crystalline aluminum film has an almost perfectly flat surface, whereas the evaporated multicrystalline film shows serious surface corrugation. Within the scanned area of 1 × 1 μm^2, the root-mean-square roughness for single- and multicrystalline aluminum film is 0.3 and 2.5 nm, respectively. We note that the unprotected aluminum surface of the single-crystalline film can actually last for a long time in the ambient environment. Although the surface does become rougher due to oxidation of aluminum and collection of dust, the surface remains much smoother than multicrystalline film after a long time. After 18 months storage in ambient conditions, the root-mean-square noise of the single-crystalline aluminum surface increases to 1.2 nm, which is still lower than that of the best electron-gun evaporated aluminum film we can prepare. The superior long-term stability is also one of the benefits of using single-crystalline aluminum film for plasmonics. The evidence of single-crystallinity of the aluminum film is provided by the selective area electron diffraction (SAED) pattern, as shown in Figure 1c. Figure 1d shows the reflectivity spectra of the single- and multicrystalline aluminum films, which give information on the overall optical response. It can be clearly seen that the MBE-grown single-crystalline aluminum film shows higher reflectivity in the UV to NIR spectral regime compared to the multicrystalline one. For a spectral window below 300 nm, the reflectance of the single-crystalline film is even up to 35% higher than that of the multicrystalline one. The ultrasmooth surface of the single-crystalline film is of key importance

for the superior reflectivity because rough surface can lead to random scattering and increased absorption. The dip in the reflectivity around 820 nm for both curves is due to the absorption of aluminum.

To further compare the flatness and the film quality, we have measured the TPPL from the two aluminum films under the same excitation power (4.5 mW on sample). Such examination is based on the fact that TPPL is very sensitive to the local field gradient. Typically, a smooth metal surface generates much lower TPPL than a rough one because it offers no nanoscale defects and thus no hot spots. The sensitivity of TPPL to the surface roughness is briefly explained in the following. In general, TPPL starts from sequential absorption of two photons and ends up with radiative recombination of the electron and hole pair. The absorption of the first photon includes an intraband transition of electron and requires momentum matching. Strong optical near-fields in resonant plasmonic nanostructures or hot spots on rough surfaces can provide high field gradient and thus broad momentum spectrum to fulfill the momentum matching condition.[39] As a result, rough surface can generate very strong TPPL, whereas an ultrasmooth surface can hardly generate TPPL. For this reason, TPPL is sensitive to local hot spots and has been used to study shape-dependent LSPR[36] and surface roughness of metallic films.[30] As shown in Figure 1e, TPPL is indeed highly enhanced by the rough surface of the multicrystalline aluminum film. In contrast, the TPPL from the atomically flat single-crystalline aluminum film is almost absent, confirming the perfect surface quality. From a fabrication point of view, the MBE method is beneficial because it allows for precise control of film thickness. The single-crystallinity also facilitates the FIB fabrication of complex plasmonic networks containing nanoscale fine features over a microscale area.[30] As can be seen in Figure 1a, long and narrow nanoslits can be easily fabricated on the single-crystalline aluminum film without a single defect. Such high-definition structures are very difficult to fabricate by applying FIB onto the multicrystalline aluminum film because the random crystal grains and surface roughness introduce variation of the resistance to the ion-beam milling and therefore result in unpredictable structural defects. It is worth noting that the Ga ion implantation into the aluminum film during FIB milling is much more serious compared to gold.[30] We have observed implantation of the Ga ion up to one-third of the aluminum atomic composition (Figure S2, Supporting Information). Such Ga ion implantation can possibly lead to significant modification of the local dielectric function of aluminum and result in difference between spectra obtained from optical experiments and numerical simulations, in which permittivity from bulk pure aluminum is used.

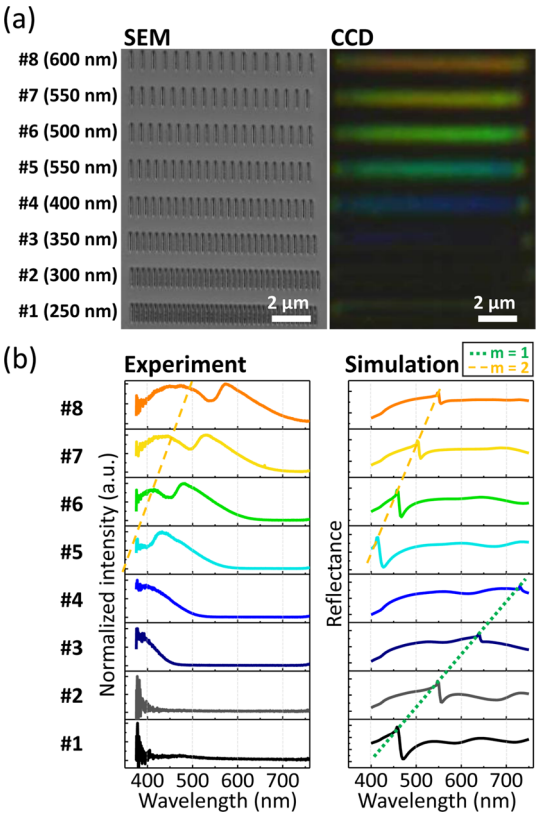

Figure 2. (a) Left panel: SEM image of the periodic nanoslit arrays numbered #1 to #8 with periodicity ranging from 250 to 600 nm. Right panel: Corresponding dark-field scattering image of the arrays. Scale bar: 2 μm. (b) Experimental dark-field scattering spectra (left) and the simulated reflectance spectra (right), showing the fundamental mode (m = 1, green dotted line) and the first higher-order mode (m = 2, orange dashed line).

UV to NIR Surface Plasmon Resonance of Nanoslit Arrays. To demonstrate UV to NIR surface plasmon resonance, we first examine the scattering of aluminum nanoslit arrays using a home-built dark-field microscope (Figure S3, Supporting Information). Because our GaAs substrate is not transparent, we illuminate the sample and collect the scattered light from the same side. Figure 2a shows the SEM images and the dark-field scattering image of eight periodic nanoslit arrays fabricated on the single-crystalline aluminum film on top of GaAs substrate. These nanoslit arrays are marked as array #1 to array #8 with increasing periodicity from 250 to 600 nm in steps of 50 nm. The gap width and the length of the slits are 40 nm and 1 μm, respectively. The interarray distance is set to 1 μm. The periodic nanoslit arrays serve as efficient couplers that provide the needed momentum for the free-space photons to excite SPPs. The coupling condition is described by Bloch equation as[40]

$$k_0 \sin\theta \pm m2\pi/P = k_0\sqrt{\frac{\varepsilon_m\varepsilon_d}{\varepsilon_m+\varepsilon_d}} \quad (1)$$

where k_0 is the wavenumber of light in a vacuum, θ is the incident angle, m is the grating order, and P is the

periodicity; ε_m and ε_d are the permittivity of aluminum and the dielectric, respectively. As the periodicity of the nanoslit array decreases, the dark-field scattering images show clear evolution of color from orange to blue and eventually dark due to the low sensitivity of the color CCD. The scattering spectra of the nanoslit arrays are shown in Figure 2b with the corresponding simulated spectra shown in the right panel. For the nanoslit arrays used in this work, two resonances corresponding to the fundamental (m = 1) and first higher-order (m = 2) resonance are observed within the observation window between 350 and 800 nm. In the simulated spectra, both resonances are clearly seen and gradually red shift as the periodicity increases, as described by eq 1. However, the fundamental resonance (m = 1) is missing in the experimental spectra. This is due to the fact that the scattering angle of the fundamental mode is the same as the incident angle. Therefore, the fundamental mode is completely blocked by the pinhole and cannot be observed (Figure S4, Supporting Information). Using a dedicated setup for signals in the UV regime, plasmonic resonance below 400 nm can be clearly observed (Figure S5, Supporting Information). In both the experimental spectra and simulated spectra, asymmetric Fano-like spectral profiles are observed. Such asymmetric line shape is due to the coupling between the broad resonance of the single slits and the relatively sharp resonance of the nanoslit array[41] (Figure S6, Supporting Information). In general, the simulations well reproduce the trend of the experimental spectra as a function of the structural geometry. Slight differences in peak position and width might be attributed to the following reasons. First, in the experiment, the incident angle of the illumination actually covers a range of about 5° but not at a specified angle as set for the plane wave excitation in the finite-difference time-domain (FDTD) simulations. Second, the spectra shown here are collected using an optical setup optimal for the vis range. This vis set of optics has relatively large loss in the UV regime. Therefore, the experimental spectra show a peak width in the UV regime slightly larger than that in the simulated ones. Using a set of optics optimized for the UV regime, the position and the width of resonance peaks indeed agree very well with the simulations. Third, the structural imperfection and the modified material properties due to Ga ion implantation can also lead to shifting and broadening of the plasmonic resonance peaks. We have done our best to mimic the rounded corners and Al_2O_3 layer in the simulations. However, other structural imperfections, such as the uneven gap width at the top and bottom of the slits or gradually reduced diameter of the nanoholes, are hard to estimate and are not considered in the simulations. We point out that the main purpose of performing numerical simulations is to confirm the trend of the experimental spectra as a function of the structural geometry. The good agreement between the experimental and simulated spectra allows us to assign and get insight into the resonance modes. Despite the slight difference in the peak position and width, numerical simulations also provide information on the optical near-fields and help us understand the underlying physics without performing expensive near-field scanning optical microscopy.

LSPR of Single Nanoholes. Next, we examined the LSPR of single nanoholes on our single-crystalline aluminum film. Compared to solid aluminum structures, such as nanodisks,[25,27] nanospheres,[42] and nanorods,[43,44] inverse nanohole structures are easy to fabricate and are of great potential in plasmonic optical trapping.[10,45] Figure 3a shows the SEM images of all the single nanoholes on the aluminum film with corresponding dark-field scattering images on the right side. For each diameter, we have fabricated a 3 × 3 array of duplicated nanoholes. The interhole distance is set to be 3 μm in order to reduce the cross-talk between holes. The diameter of the hole is scanned from 150 to 750 nm in steps of 50 nm, resulting in 13 different nanohole diameters, marked as #1 to #13. Their scattering images show a clear red shift as the nanohole diameter increases. Dark-field scattering spectra of the nanoholes and the corresponding simulated spectra are shown in Figure 3b. The experimental spectra show two resonant modes in good agreement with the simulated scattering spectra. These two modes are the in-plane LSPR mode of the aluminum nanohole and the photonic mode of the vertical air hole in GaAs. The vertical air channel is produced because FIB is milling too deep into the GaAs substrate. Therefore, the vertical air channel in the GaAs essentially forms an out-of-plane Fabry–Pérot cavity for the photonic modes. Increasing the nanohole diameter shifts the in-plane LSPR mode from the UV regime (nanoholes #1 and #2) to the NIR regime (nanoholes #10 to #13), as marked with the red dotted lines in Figure 3b. The photonic mode in the vertical GaAs nanohole (blue dashed lines in Figure 3b) also shows a slight red shift with increasing diameter. Although the cavity length (*i.e.*, the depth of the air hole in GaAs) is rather constant for all holes, the effective index of the photonic mode slightly increases with increasing diameter. As a result, the resonance wavelength slightly red shifts with increasing diameter. In fact, such a photonic mode exists even without the aluminum film, as shown in Figure 4. Figure 4a depicts the schematic diagram of a nanohole structure used in the simulations. The nanohole (diameter = 300 nm, depth = 500 nm) is fabricated into the GaAs without and with the coverage of a 40 nm thick aluminum film. The nominal depth is defined as the distance from top surface to the bottom. Figure 4b shows the simulated scattering spectra of the nanohole fabricated in the GaAs substrate with (black

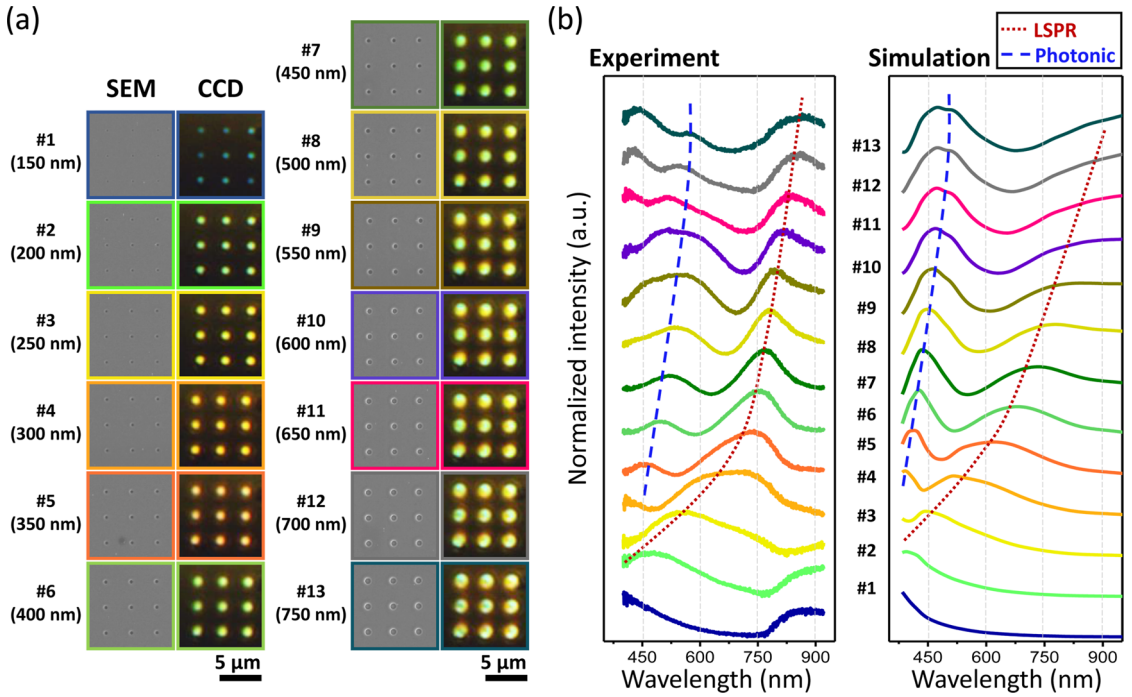

Figure 3. (a) SEM and scattering images of the single nanoholes marked by #1 to #13 with diameters ranging from 150 to 750 nm in steps of 50 nm. Scale bars: 5 μm. (b) Experimental dark-field scattering spectra (left) and simulated scattering spectra (right) of the nanoholes. Two modes due to the in-plane LSPR (red dotted line) mode and the Fabry–Pérot resonance of the photonic mode in the vertical air channel in the GaAs substrate (blue dashed line) are observed.

trace) and without (red trace) the aluminum layer. With the aluminum layer, two peaks are observed around 430 and 520 nm. However, without the aluminum film, only the peak around 430 nm is observed, suggesting that this mode is not due to LSPR of the aluminum hole. Figure 4c shows the electric near-field intensity distribution at the two resonant wavelengths. Field distributions recorded on an x–y plane 5 nm away from the aluminum or GaAs surface are shown on the top row, and the cross-sectional field distributions recorded on an x–z plane cutting through the nanohole center are shown in the bottom row in Figure 4c. From the near-field distribution, the broad peak around 520 nm (red dotted line) can be assigned exclusively to the LSPR and the sharp peak around 430 nm is due to the Fabry–Pérot resonance of the photonic modes in the vertical air channel in the GaAs substrate. As can be seen, the photonic mode in the vertical air channel in GaAs is independent of the existence of the aluminum film. The photonic mode is not seen for nanoholes with a diameter smaller than 200 nm because the mode is cut off, a clear feature of photonic modes in dielectric waveguides. The photonic mode is unique for the GaAs substrate and is less pronounced in a low-index substrate, such as glass. The presence of these two modes in one nanohole structure adds more functions to the nanohole and can be useful for applications which require interaction of two resonant modes. For example, one may trap very small particles using the enhanced optical field of the LSPR mode and use the photonic mode to enhance light–matter interaction. It is worth noting that the use of single-crystalline film is of critical importance for the observation of the trend and the identification of the two different resonances. Nanoholes on multicrystalline aluminum film contain unpredictable defects and give weaker scattering signals (Figure S7, Supporting Information).

TPPL Mapping and Polarization-Dependent TPPL Intensity. To further understand the resonance and the photoluminescence properties of plasmonic aluminum nanoholes on the GaAs substrate, we have performed TPPL mapping[30,46–48] of single nanoholes and systematically studied the relationship between the excitation polarization and the TPPL intensity. TPPL maps are generated by plotting the TPPL intensity as a function of the position of laser focus, which is raster scanned over the nanoholes in steps of 50 nm. Because the GaAs substrate also gives strong nonlinear luminescence, we have integrated only the spectrum between 570 and 590 nm in order to exclude the interference from the nonlinear signals of GaAs (Figure S8, Supporting Information). The two-photon nature of the luminescence is confirmed by the quadratic dependence of the luminescence signals on the excitation power. Figure 5a shows the TPPL intensity as a function of the nanohole diameter. The corresponding TPPL maps for single nanoholes are displayed on the top of the plot. The TPPL intensity reaches the maximum at nanoholes #4 and #5 and gradually decreases as the diameter

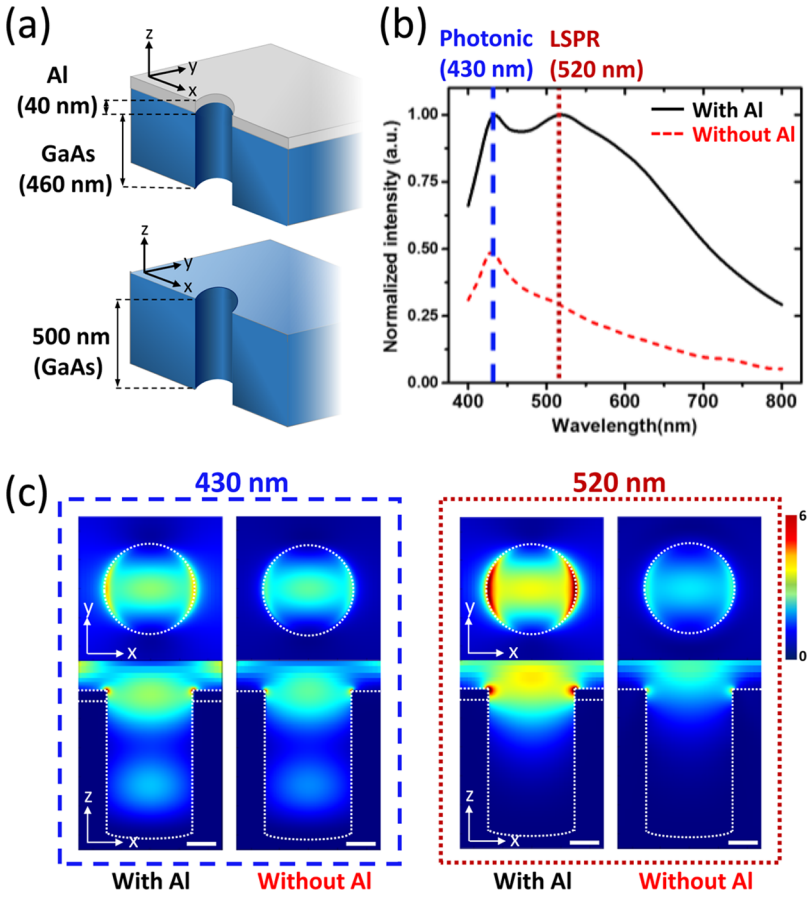

Figure 4. (a) Schematic diagram of the nanohole (diameter = 300 nm) used in the FDTD simulations. The nanohole is fabricated into the GaAs substrate with (top) and without (bottom) the coverage of a 40 nm thick aluminum film. (b) Simulated scattering spectra of the nanohole (diameter = 300 nm, depth = 500 nm) fabricated into the GaAs substrate with (black solid line) and without (red dashed line) the aluminum layer. The resonance of the photonic mode in the vertical air channel (blue dashed line at 430 nm) and the localized surface plasmon resonance (red dotted line at 520 nm) are denoted as "Photonic" and "LSPR", respectively. (c) Electric near-field intensity distribution ($I = |E_x|^2 + |E_y|^2 + |E_z|^2$) of the nanohole recorded at the resonant wavelength of the photonic mode (430 nm, left panel) and the LSPR mode (520 nm, right panel). The top row shows the intensity distribution recorded at the $x-y$ plane 5 nm above the aluminum and GaAs surface. The bottom row shows the cross-sectional intensity distribution recorded in an $x-z$ plane cutting through the center of the vertical air channel. Scale bar: 100 nm.

further increases, showing clear resonance-enhanced TPPL generation. As can be seen in the dark-field scattering spectra shown in Figure 3b, the LSPR peaks of nanoholes #4, #5, and #6 best overlap with the wavelength of the excitation laser (*i.e.*, 770 nm). This doubly confirms the relationship between TPPL generation and the diameter-dependent LSPR of the nanoholes. We have performed FDTD simulations to obtain the quadruplicate electric field ($|E|^4$) inside the aluminum in order to confirm the trend of TPPL intensity as a function of the nanohole diameter. Since TPPL is a two-photon nonlinear process, $|E|^4$ can be considered as a quantity proportional to the TPPL intensity.[30,48] As shown in Figure 5a, the results obtained from the simulations (open squares linked by black solid line) agree well with the experimental results (red solid dots).

In fact, for nanoholes with a diameter larger than 500 nm, they are able to support higher-order quadrupolar LSPR modes. Since our laser is tightly focused (spot size = 520 nm), the symmetry of the system is broken as we scan the laser focal spot through the nanohole, and the originally dark quadrupolar LSPR mode of the large holes can be excited. The excitation of the quadrupolar LSPR mode leads to the ring-shaped patterns of nanoholes #11 to #13 in the TPPL map.

To compare the dipolar and quadrupolar resonances, we take two nanoholes with diameters of 300 nm (#4) and 750 nm (#13) as examples. They represent nanoholes with diameter smaller and larger than the size of the laser focal spot. These two nanoholes support the dipolar and quadrupolar LSPR modes, respectively (Figure S9, Supporting Information). The excitation power for nanohole #13 has been increased to 3 mW, that is, 3 times larger than the power used for nanohole #4, in order to clearly visualize the TPPL pattern. Upon our laser excitation, the two nanoholes show distinct patterns in the TPPL map, as shown in Figure 5b,c. For the nanohole #4, a single maximum

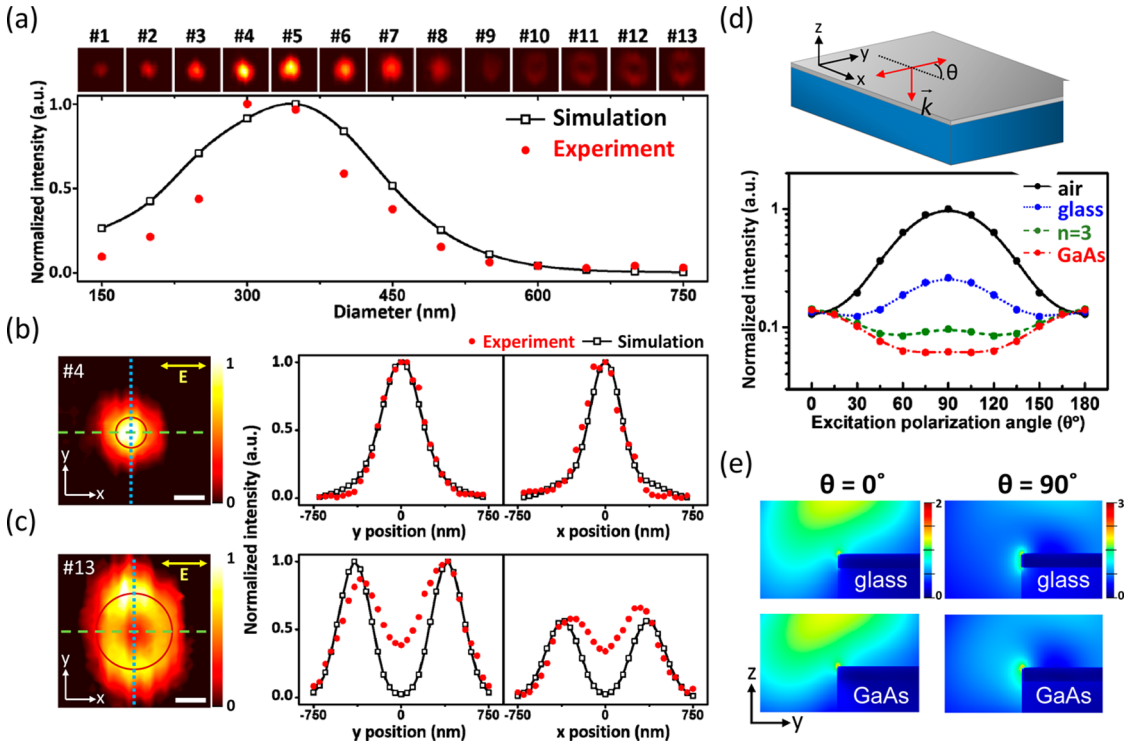

Figure 5. (a) Top row: TPPL intensity maps of nanoholes #1 to #13 with a scanning size of 1.5 × 1.5 μm^2. Bottom row: Normalized maximum intensity in the experimental TPPL intensity maps (red dots) and the calculated $|E|^4$ (black open squares) with respect to the nanohole diameter. (b,c) Left panels: Intensity maps of the nanoholes with diameters of 300 nm (#4) and 750 nm (#13), respectively. Scale bars: 300 nm. Right panels: Corresponding intensity profiles of the normalized experimental (red dots) and simulated intensity (black open squares) along the lines in *x*- (green dashed line) and *y*-direction (blue dotted line) cutting through the nanohole intensity maps. (d) Calculated $|E|^4$ and excitation polarization dependence on an infinite straight edge with different substrates. (e) Electric near-field distributions around the edge of an aluminum film (thickness = 40 nm) on glass (top) and GaAs (bottom) under excitation with polarization along the *x*-direction ($\theta = 0°$, left) and *y*-direction ($\theta = 90°$, right).

of the TPPL intensity is obtained as the laser spot is scanned through the center of the nanohole, revealing a dipolar LSPR resonance. For the nanohole #13, interestingly, a ring-shaped intensity distribution with slightly higher intensity at the top and bottom edges in the *y*-direction is observed (Figure 5c). Since our excitation is polarized in the *x*-direction, such observation of relatively high TPPL intensity in the *y*-direction is counterintuitive. Typically, laser excitation with polarization perpendicular to the edge of the hole is expected to be more efficient in exciting TPPL compared to excitation with polarization parallel to the edge.[49] Therefore, one would intuitively expect that the two-lobe pattern is along the *x*-direction instead of the *y*-direction. The right panels of Figure 5b,c show the line-cut profiles of the experimental TPPL maps and the simulated $|E|^4$ profiles along the same lines in *x*- and *y*-direction. For both holes, the simulated line-cut profiles are in good agreement with the experimental ones and the counterintuitive pattern for nanohole #13 is reproduced.

To understand this pattern, we first make sure that the counterintuitive two-lobe pattern of the 750 nm nanohole is not due to the laser scanning direction or the structural asymmetry due to FIB milling. For this purpose, we have changed the excitation polarization to the *y*-direction and have observed that the two-lobe pattern changes accordingly; that is, higher intensity is now found in the *x*-direction. This confirms that the counterintuitive two-lobe pattern is purely determined by the polarization of the excitation. Next, we perform a series of simulations to examine the trend of $|E|^4$ as a function of the laser polarization angle with respect to the edge of the aluminum film.

Four different substrates are used in the simulations, including air, glass, a hypothetical substrate (n = 3.0), and the GaAs (n = 3.7 + 0.092i). An infinitely extended straight edge of an aluminum film (thickness = 40 nm) is used as a model structure to reflect the excitation efficiency of a polarized illumination at the film edge. The extended straight edge and the excitation geometry are depicted in the top panel of Figure 5d. For each substrate, we illuminate the edge of the aluminum film with a Gaussian beam (NA = 0.9) and simulate the $|E|^4$ in the aluminum material as a function of the excitation polarization angle (θ) with respect to the *x*-direction ($\theta = 0°$). Figure 5d shows that, for different substrates, the $|E|^4$ in the aluminum film exhibits different dependence on the polarization

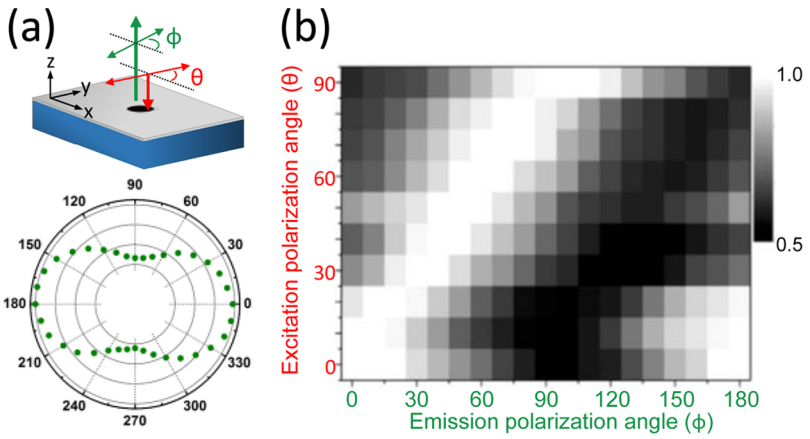

Figure 6. (a) Top: Schematic diagram of the excitation (θ) and emission polarization (ϕ). Bottom: Polar plot showing the emission polarization of the TPPL from the nanohole #4 (diameter = 300 nm) under *x*-polarized excitation ($\theta = 0°$). The DoLP of the TPPL is about 0.38. (b) Polarization correlation plot of the TPPL from aluminum nanohole #4.

angle. As the refractive index of the substrate increases, the $|E|^4$ inside the aluminum decreases rapidly if the excitation is polarized in the *y*-direction ($\theta = 90°$), that is, perpendicular to the edge. The $|E|^4$ under excitation polarized along the *x*-axis ($\theta = 0°$), that is, parallel to the edge, is rather insensitive to the change of substrate. For a free aluminum film in air or on top of a glass substrate, the maximum of $|E|^4$ is obtained with excitation polarization perpendicular to the film edge ($\theta = 90°$), as would be normally expected. However, for the hypothetical substrate and the GaAs substrate, the $|E|^4$ is severely suppressed when the excitation polarization is perpendicular to the edge. As a result, the relatively large $|E|^4$ and relatively pronounced TPPL are obtained when the excitation polarization is parallel to the edge. This explains the counterintuitive two-lobe pattern observed in the TPPL pattern of the 750 nm hole. By further examining the simulated near-field distribution (Figure 5e), we found that the spatial distribution of the excited near-field is strongly dependent on the excitation polarization. This is due to the fact that excitation with different polarization couples differently into the aluminum film. For excitation polarization perpendicular to the edge ($\theta = 90°$), the field couples more into the aluminum film compared to the case with excitation polarization parallel to the edge ($\theta = 0°$). Therefore, the index of the substrate has a relatively large influence on the field. Since the GaAs substrate is highly absorbing, it dampens the electromagnetic field more severely under perpendicularly polarized excitation. Consequently, the counterintuitive two-lobe pattern is obtained. Such a property is unique for the high-index GaAs substrate and needs to be considered in the design of plasmonic structures. Here, we note that the use of single-crystalline aluminum film is the key for the observation of such a counterintuitive TPPL pattern because the ultrasmooth surface and the nearly perfect rim of the hole produce extremely low background noise (Figure 1d) and therefore guarantee successful observation of the small difference in the intensity of the TPPL pattern.

Finally, we study the polarization of the TPPL from aluminum. Aluminum has been reported to preserve the excitation polarization.[43] In this work, we perform polarization analysis of TPPL using the nanohole #4 (diameter = 300 nm). Since this nanohole is radially symmetric, we can rule out any possible contribution from the anisotropy of structural geometry to the fluctuation of TPPL intensity. Figure 6a shows the emission polar plot of the TPPL from the nanohole excited with illumination polarized along the *x*-direction ($\theta = 0°$). A degree of linear polarization (DoLP) of about 0.38 is obtained for the emission, suggesting that the TPPL from the aluminum hole is preferably polarized along the excitation polarization. By plotting the emission polarization-dependent intensity as a function of the excitation polarization, we have obtained a polarization correlation plot, as shown in Figure 6b. It can be seen that the emission polarization of TPPL follows the polarization of the excitation, giving direct evidence that the aluminum TPPL preserves the polarization of the excitation. It is worth noting that the total intensity of the TPPL does not vary with the excitation polarization, meaning that the TPPL yield of aluminum is independent of the crystallinity of our single-crystalline aluminum film.

CONCLUSION

We have presented single-crystalline aluminum nanostructures on aluminum film grown with the MBE method on top of a high-index GaAs substrate. We demonstrate clear plasmonic resonance in the UV to NIR spectral regime. With TPPL intensity mapping, we found a counterintuitive TPPL pattern that shows relatively high TPPL yield with excitation polarization parallel to the edge of the aluminum film. The counterintuitive pattern is found to relate to the high index of the GaAs substrate. With our single-crystalline

TABLE 1. Details of the Optics Used for the Detection of UV and Visible Signals

	wavelength range (nm)	microscope objective	achromatic lens	reflection mirrors	spectrometer grating settings
UV	300−600	LMU-40X-UVB, air, NA = 0.5, Thorlabs	NUDL-50-300P, SIGMA KOKI	aluminum mirrors, PF10-03-F01, Thorlabs	300 lines/mm, blaze at 300 nm
visible	450−850	MPlanApo 60×, air, NA = 0.9, Olympus	AC254-300-A-ML, f = 300 mm, Thorlabs	silver mirrors, PF10-03-P01, Thorlabs	150 lines/mm, blaze at 800 nm

aluminum film and the radially symmetric nanohole structure, we confirm that the polarization of TPPL from aluminum depends mainly on the excitation polarization but not on the crystallinity of the metal or substrate. Aluminum nanohole structures can be easily fabricated and are useful for optical trapping or manipulation. High-quality single-crystalline aluminum film is of great potential for the realization of complex integrated plasmonic optical nanocircuits[5,30] and plasmonic nanolasers.[31] We anticipate applications of single-crystalline aluminum plasmonic nanostructures in broadband and CMOS-compatible plasmonic photodetectors and other nanophotonic devices operating in the UV to NIR regime.

MATERIALS AND METHODS

SEM, FIB, and SAED Parameters. SEM images were taken with a beam voltage of 30 kV and current of 0.17 nA. Two settings were used for FIB milling. For fine structures like the nanoslits in Figure 2a, acceleration voltage of 30 kV and beam current of 7.7 pA were used. For large-area milling, 30 kV and 80 pA were used to gain etching speed. The sample for SEAD was prepared by mechanical polish followed by FIB milling. The polishing procedure was kept below 150 °C to avoid any annealing. The SAED was performed with a field emission gun (JEOL, JEM-2100F) at room temperature on the cross section of the aluminum film on the GaAs substrate.

Dark-Field Microscopy. A home-built confocal dark-field microscope was used to obtain the scattering spectra of the nanostructures (Figure S3, Supporting Information). Briefly, a ring-shaped nonpolarized broadband white light (HAL 100 illuminator with quartz collector, Zeiss) was collimated and concentrated onto the sample plane by a microscope objective. The scattered light was then collected by the same objective and aligned by an achromatic lens onto the imaging CCD or the entrance slit of a UV−vis spectrometer (SR-303i-A with DU401A-BV CCD, Andor) for spectral analysis. The straight scattering of the excitation is blocked by a beam stop with a small pinhole (diameter = 4 mm) at the center. Two sets of optics optimal for the signals in the UV and visible windows were used in order to obtain optimal detection efficiency. For the clarity of presentation, results obtained with the visible optics set are presented in the main text and the results from the UV set are in Figure S5 in the Supporting Information. Details of the two sets of optics are summarized in Table 1. All spectra have been normalized to the wavelength-dependent quantum efficiency of the CCD detector.

Setup for TPPL Mapping and Spectral Analysis. A home-built laser scanning microscope was used for all TPP mapping experiments. The setup is depicted in Figure S3 of Supporting Information. To excite the TPPL, laser pulses from a Ti:sapphire laser (center wavelength = 770 nm, pulse duration = 140 fs, repetition = 80 MHz, Chameleon Ultra II) were filtered by a long-pass filter (FEL0750, Thorlabs), reflected by a dichroic mirror (FF720-SDi01, Semrock), and focused onto the sample plane by a near-infrared microscope objective (100× NeoSPlan NIC, NA = 0.9, Olympus). A half-wave plate (AHWP10M-980, Thorlabs) prior to the objective was used to control the excitation polarization prior to the objective. The generated TPPL was collected by the same objective, passing through the dichroic mirror, filtered by a short-pass filter (λ < 690 nm, XVS0690, Asahi), and aligned into the entrance slit of the spectrometer (Acton SP2750, Princeton Instruments). To avoid intensity difference due to the discriminative grating efficiency on the polarization, we used a second half-wave plate (AHWP10M-600, Thorlabs) and a linear polarizer to control the polarization of the emission prior to the spectrometer so that the spectral analysis of TPPL was performed under identical grating efficiency. The averaged excitation power was kept at 1 mW, and the exposure time of the CCD equipped on the spectrometer was 1.0 s. The sample was mounted on a piezo stage with a close-loop feedback control (P-611.3S stage and E-664 controller, Physik Instrumente). Spatial-resolved TPPL mapping images were obtained by scanning the sample position (step size: 50 nm) and plotting the integrated TPPL intensity (integration spectral window: 570−590 nm) with respect to the excitation position.

Numerical Simulations. Numerical simulations were performed with finite-difference time-domain method (FDTD Solutions, Lumerical Solutions). To obtain the far-field scattering spectra of the periodic nanoslits, we simulated the reflectance of the nanoslit array. The configuration of the simulation is shown in Figure S10 in the Supporting Information. The polarization of the plane wave source was perpendicular to the nanoslits, and the incident angle was set to be 25° and 55° to mimic the experimental incident conditions determined by the numerical aperture of the objectives for UV and visible light, respectively. Bloch boundary condition was used for periodic structures. For nanoholes, the total-field scattered-field source with a wavelength ranging from 300 to 900 nm was used to obtain the scattering spectra. The source was set to be normally incident because the LSPRs of single nanoholes are independent of the incident angle. Perfectly matched layer boundaries were placed at least 1 μm away from the nanoholes. The scattering spectra were obtained by integrating the Poynting vector over the area of a two-dimensional monitor, which was 600 nm above the nanostructure. All simulated spectra were normalized to the source spectrum. To simulate the generation efficiency of the TPPL as a function of excitation position, we used a tightly focused Gaussian source synthesized by a thin lens setting (NA = 0.9 approximated by 200 plane waves). Square of the simulated electric field intensity $|E|^4$ was then integrated over the whole volume of metal to obtain a quantity proportional to the TPPL intensity. For all structures, the aluminum film with a thickness of 40 nm, including an oxide layer of 2 nm and an aluminum layer of 38 nm, was placed on the GaAs substrate. Rounded corners (radius of curvature = 5 nm) were used to mimic the actual geometry of the nanostructures fabricated by FIB milling. The dielectric functions of Al, Al_2O_3, and GaAs were modeled with experimental data from Palik.[50]

Conflict of Interest: The authors declare no competing financial interest.

Acknowledgment. Support from the Ministry of Science and Technology of Taiwan under Grant Nos. NSC-101-2113-M-007-002-MY2, NSC-101-2628-E-009-MY3, and MOST-103-2113-M-007-004-MY3 is gratefully acknowledged. S.D.L. acknowledges the financial support from MOST and from ATU program of MOE

in Taiwan. The equipment support from CNST and NFC at NCTU is appreciated. J.S.H. thanks the support from the Center for Nanotechnology, Materials Sciences, and Microsystems at National Tsing Hua University.

Supporting Information Available: XRD analysis, EDX analysis, experimental setup, objective collection efficiency, UV spectra, Fano-like resonance of nanoslits array, comparison of scattering spectra, TPPL spectrum, mode analysis, and FDTD settings. This material is available free of charge via the Internet at http://pubs.acs.org.

REFERENCES AND NOTES

1. Biagioni, P.; Huang, J.-S.; Hecht, B. Nanoantennas for Visible and Infrared Radiation. *Rep. Prog. Phys.* **2012**, *75*, 024402.
2. Novotny, L.; van Hulst, N. Antennas for Light. *Nat. Photonics* **2011**, *5*, 83–90.
3. Ebbesen, T. W.; Genet, C.; Bozhevolnyi, S. I. Surface-Plasmon Circuitry. *Phys. Today* **2008**, *61*, 44–50.
4. Hung, Y.-T.; Huang, C.-B.; Huang, J.-S. Plasmonic Mode Converter for Controlling Optical Impedance and Nanoscale Light–Matter Interaction. *Opt. Express* **2012**, *20*, 20342–20355.
5. Dai, W.-H.; Lin, F.-C.; Huang, C.-B.; Huang, J.-S. Mode Conversion in High-Definition Plasmonic Optical Nanocircuits. *Nano Lett.* **2014**, *14*, 3881–3886.
6. Liu, W.-L.; Lin, F.-C.; Yang, Y.-C.; Gwo, S.; Huang, M. H.; Huang, J.-S. The Influence of Shell Thickness of Au@TiO_2 Core–Shell Nanoparticles on Plasmonic Enhancement Effect in Dye-Sensitized Solar Cells. *Nanoscale* **2013**, *5*, 7953–796.
7. Stewart, M. E.; Anderton, C. R.; Thompson, L. B.; Maria, J.; Gray, S. K.; Rogers, J. A.; Nuzzo, R. G. Nanostructured Plasmonic Sensors. *Chem. Rev.* **2008**, *108*, 494–521.
8. Anker, J. A.; Hall, W. P.; Lyandres, O.; Shah, N. C.; Zhao, J.; Duyne, R. P. V. Biosensing with Plasmonic Nanosensors. *Nat. Mater.* **2008**, *7*, 442–453.
9. Lin, D.; Huang, J.-S. Slant-Gap Plasmonic Nanoantennas for Optical Chirality Engineering and Circular Dichroism Enhancement. *Opt. Express* **2014**, *22*, 7434–7445.
10. Pang, Y.; Gordon, R. Optical Trapping of a Single Protein. *Nano Lett.* **2012**, *12*, 402–406.
11. Chen, K.-Y.; Lee, A.-T.; Hung, C.-C.; Huang, J.-S.; Yang, Y.-T. Transport and Trapping in Two-Dimensional Nanoscale Plasmonic Optical Lattice. *Nano Lett.* **2013**, *13*, 4118–4122.
12. Hogan, N. J.; Urban, A. S.; Ayala-Orozco, C.; Pimpinelli, A.; Nordlander, P.; Halas, N. J. Nanoparticles Heat through Light Localization. *Nano Lett.* **2014**, *14*, 4640–4645.
13. Sobhani, A.; Knight, M. W.; Wang, Y.; Zheng, B.; King, N. S.; Brown, L. V.; Fang, Z.; Nordlander, P.; Halas, N. J. Narrowband Photodetection in the Near-Infrared with a Plasmon-Induced Hot Electron Device. *Nat. Commun.* **2013**, *4*, 1643.
14. Shrestha, V. R.; Lee, S.-S.; Kim, E.-S.; Choi, D.-Y. Aluminum Plasmonics Based Highly Transmissive Polarization-Independent Subtractive Color Filters Exploiting a Nanopatch Array. *Nano Lett.* **2014**, *14*, 6672–6678.
15. Sun, Y.; Xia, Y. Shape-Controlled Synthesis of Gold and Silver Nanoparticles. *Science* **2002**, *298*, 2176–2179.
16. Chiu, C.-Y.; Chung, P.-J.; Lao, K.-U.; Liao, C.-W.; Huang, M. H. Facet-Dependent Catalytic Activity of Gold Nanocubes, Octahedra, and Rhombic Dodecahedra toward 4-Nitroaniline Reduction. *J. Phys. Chem. C* **2012**, *116*, 23757–23763.
17. Vakil, A.; Engheta, N. Transformation Optics Using Graphene. *Science* **2011**, *332*, 1291–1294.
18. Fei, Z.; Rodin, A. A.; Gannett, W.; Dai, S.; Regan, W.; Wager, M.; Liu, M. K.; McLeod, A. S.; Dominguez, G.; Thiemens, M.; et al. Electronic and Plasmonic Phenomena at Graphene Grain Boundaries. *Nat. Nanotechnol.* **2013**, *8*, 821–825.
19. Boltasseva, A.; Atwater, H. A. Low-Loss Plasmonic Metamaterials. *Science* **2011**, *331*, 290.
20. Naik, G. V.; Schroeder, J. L.; Ni, X.; Kildishev, A. V.; Sands, T. D.; Boltasseva, A. Titanium Nitride as a Plasmonic Material for Visible and Near-Infrared Wavelengths. *Opt. Mater. Express* **2012**, *2*, 478–489.
21. Kinsey, N.; Ferrera, M.; Naik, G. V.; Babicheva, V. E.; Shalaev, V. M.; Boltasseva, A. Experimental Demonstration of Titanium Nitride Plasmonic Interconnects. *Opt. Express* **2014**, *22*, 12238–12247.
22. McMahon, J. M.; Schatz, G. C.; Gray, S. K. Plasmonics in the Ultraviolet with the Poor Metals Al, Ga, In, Sn, Ti, Pb, and Bi. *Phys. Chem. Chem. Phys.* **2013**, *15*, 5415–5423.
23. Ray, K.; Chowdhury, M. H.; Lakowicz, J. R. Aluminum Nanostructured Flms as Substrates for Enhanced Fluorescence in the Ultraviolet-Blue Spectral Region. *Anal. Chem.* **2007**, *79*, 6480–6487.
24. Mahdavi, F.; Blair, S. Nanoaperture Fluorescence Enhancement in the Ultraviolet. *Plasmonics* **2010**, *5*, 169–174.
25. Langhammer, C.; Schwind, M.; Kasemo, B.; Zoric, I. Localized Surface Plasmon Resonances in Aluminum Nanodisks. *Nano Lett.* **2008**, *8*, 1461–1471.
26. Knight, M. W.; Liu, L. F.; Wang, Y. M.; Brown, L.; Mukherjee, S.; King, N. S.; Everitt, H. O.; Nordlander, P.; Halas, N. J. Aluminum Plasmonic Nanoantennas. *Nano Lett.* **2012**, *12*, 6000–6004.
27. Knight, M. W.; King, N. S.; Liu, L.; Everitt, H. O.; Nordlander, P.; Halas, N. J. Aluminum for Plasmonics. *ACS Nano* **2014**, *8*, 834–840.
28. Zheng, B. Y.; Wang, Y.; Nordlander, P.; Halas, N. J. Color-Selective and CMOS-Compatible Photodetection Based on Aluminum Plasmonics. *Adv. Mater.* **2014**, *26*, 6318–6323.
29. Kuttge, M.; Vesseur, E. J. R.; Verhoeven, J.; Lezec, H. J.; Atwater, H. A.; Polman, A. Loss Mechanisms of Surface Plasmon Polaritons on Gold Probed by Cathodoluminescence Imaging Spectroscopy. *Appl. Phys. Lett.* **2008**, *93*, 113110.
30. Huang, J.-S.; Callegari, V.; Geisler, P.; Brüning, C.; Kern, J.; Prangsma, J. C.; Wu, X.; Feichtner, T.; Ziegler, J.; Weinmann, P.; et al. Atomically Flat Single-Crystalline Gold Nanostructures for Plasmonic Nanocircuitry. *Nat. Commun.* **2010**, *1*, 150.
31. Lu, Y. J.; Kim, J.; Chen, H. Y.; Wu, C. H.; Dabidian, N.; Sanders, C. E.; Wang, C. Y.; Lu, M. Y.; Li, B. H.; Qiu, X. G.; et al. Plasmonic Nanolaser Using Epitaxially Grown Silver Film. *Science* **2012**, *337*, 450–453.
32. Levine, I.; Yoffe, A.; Salomon, A.; Li, W.; Feldman, Y.; Cahen, D.; Vilan, A. Epitaxial Two Dimensional Aluminum Films on Silicon (111) by Ultra-fast Thermal Deposition. *J. Appl. Phys.* **2012**, *111*, 124320.
33. Stefaniuk, T.; Wróbel, P.; Ciesielski, A.; Szoplik, T. Fabrication of Smooth Al Nanolayers at Different Temperatures. *15th International Conference on Transparent Optical Networks*; June 23–27, **2013**, Cartagena, Colombia; DOI: 10.1109/ICTON.2013.6602895; Tu.P.26.
34. Sigle, D. O.; Perkins, E.; Baumberg, J. J.; Mahajan, S. Reproducible Deep-UV SERRS on Aluminum Nanovoids. *J. Phys. Chem. Lett.* **2013**, *4*, 1449–1452.
35. Aspnes, D. E.; Kinsbron, E.; Bacon, D. D. Optical Properties of Au: Sample Effects. *Phys. Rev. B* **1980**, *21*, 3290–3299.
36. Chen, W.-L.; Lin, F.-C.; Lee, Y.-Y.; Li, F.-C.; Chang, Y.-M.; Huang, J.-S. The Modulation Effect of Transverse, Antibonding, and Higher-Order Longitudinal Modes on the Two-Photon Photoluminescence of Gold Plasmonic Nanoantennas. *ACS Nano* **2014**, *8*, 9053–9062.
37. Chang, C.-W.; Lin, F.-C.; Chiu, C.-Y.; Su, C.-Y.; Huang, J.-S.; Perng, T.-P.; Yen, T.-J. HNO_3^-Assisted Polyol Synthesis of Ultralarge Single-Crystalline Ag Microplates and Their Far Propagation Length of Surface Plasmon Polariton. *ACS Appl. Mater. Interfaces* **2014**, *6*, 11791–11798.
38. Lin, S.-W.; Wu, J.-Y.; Lin, S.-D.; Lo, M.-C.; Lin, M.-H.; Liang, C.-T. Characterization of Single-Crystalline Aluminum Thin Film on (100) GaAs Substrate. *Jpn. J. Appl. Phys.* **2013**, *52*, 045801.
39. Beversluis, M. R.; Bouhelier, A.; Novotny, L. Continuum Generation from Single Gold Nanostructures through Near-Field Mediated Intraband Transitions. *Phys. Rev. B* **2003**, *68*, 115433.

40. Barnes, W. L.; Murray, W. A.; Dintinger, J.; Devaux, E.; Ebbesen, T. W. Surface Plasmon Polaritons and Their Role in the Enhanced Transmission of Light through Periodic Arrays of Subwavelength Holes in a Metal Film. *Phys. Rev. Lett.* **2004**, *92*, 107401.
41. Lee, K. L.; Chen, P. W.; Wu, S. H.; Huang, J. B.; Yang, S. Y.; Wei, P. K. Enhancing Surface Plasmon Detection Using Template-Stripped Gold Nanoslit Arrays on Plastic Films. *ACS Nano* **2012**, *6*, 2931–2939.
42. Sanz, J. M.; Ortiz, D.; Alcaraz de la Osa, R.; Saiz, J. M.; González, F.; Brown, A. S.; Losurdo, M.; Everitt, H. O.; Moreno, F. UV Plasmonic Behavior of Various Metal Nanoparticles in the Near- and Far-Field Regimes: Geometry and Substrate Effects. *J. Phys. Chem. C* **2013**, *117*, 19606–19615.
43. Castro-Lopez, M.; Brinks, D.; Sapienza, R.; van Hulst, N. F. Aluminum for Nonlinear Plasmonics: Resonance-Driven Polarized Luminescence of Al, Ag, and Au Nanoantennas. *Nano Lett.* **2011**, *11*, 4674–4678.
44. Schwab, P. M.; Moosmann, C.; Wissert, M. D.; Schmidt, E. W.-G.; Ilin, K. S.; Siegel, M.; Lemmer, U.; Eisler, H.-J. Linear and Nonlinear Optical Characterization of Aluminum Nanoantennas. *Nano Lett.* **2013**, *13*, 1535–1540.
45. Berthelot, J.; Aćimović, S. S.; Juan, M. L.; Kreuzer, M. P.; Renger, J.; Quidant, R. Three-Dimensional Manipulation with Scanning Near-Field Optical Nanotweezers. *Nat. Nanotechnol.* **2014**, *9*, 295–299.
46. Imura, K.; Nagahara, T.; Okamoto, H. Near-Field Two-Photon-Induced Photoluminescence from Single Gold Nanorods and Imaging of Plasmon Modes. *J. Phys. Chem. B* **2005**, *109*, 13214–13220.
47. Viarbitskaya, S.; Teulle, A.; Marty, R.; Sharma, J.; Girard, C.; Arbouet, A.; Dujardin, E. Tailoring and Imaging the Plasmonic Local Density of States in Crystalline Nanoprisms. *Nat. Mater.* **2013**, *12*, 426–432.
48. Huang, J.-S.; Kern, J.; Geisler, P.; Weinmann, P.; Kamp, M.; Forchel, A.; Biagioni, P.; Hecht, B. Mode Imaging and Selection in Strongly Coupled Nanoantennas. *Nano Lett.* **2010**, *10*, 2105–2110.
49. Xu, T.; Wu, Y.-K.; Luo, X.; Guo, L. J. Plasmonic Nanoresonators for High-Resolution Colour Filtering and Spectral Imaging. *Nat. Commun.* **2010**, *1*, 59.
50. Palik, E. D. *Handbook of Optical Constants of Solids*; Academic Press: Orlando, FL, 1985; Vol. I.